On the Possibility of Using ULF/ELF Electromagnetic Waves from Undersea Cables to Detect Airplanes Submerged in the Ocean

Dallin R. Smith [1] and Jamesina J. Simpson [2]

[1] Air Force Research Labs
Albuquerque, NM 87117, USA
dallin@afrlnewmexico.com

[2] Department of Electrical and Computer Engineering
University of Utah, Salt Lake City, UT 84112, USA
jamesina.simpson@utah.edu

Abstract ─ The loss of Malaysian Flight on March 8, 2014, and the subsequent lengthy search for the aircraft highlights the need for an effective detection system for locating airplanes that have crashed into the ocean. The goal of this paper is to test the feasibility of detecting submerged airplanes using ultra-low frequency and/or extremely-low frequency electromagnetic signals generated by undersea cables located along the bottom of the ocean. The proposed detection system is tested using three-dimensional finite-difference time-domain (FDTD) modeling of the cable source, ocean water, ground, and submerged object (aircraft). The perturbation caused by the object is obtained for different positions of the object relative to the cable source. The magnitude of the perturbation is compared to the expected background level for a depth of 3 km into the ocean. A sensor array is proposed for detecting objects within several km of the cable.

Index Terms ─ Airplane, extremely-low frequency, FDTD, ocean, ultra-low frequency.

I. INTRODUCTION

Malaysian Flight 370 (MH370) took off at 12:42 AM on March 8, 2014, and disappeared from air-traffic control secondary radar 39 minutes later. Later, a study of primary radar data indicated that MH370 flew off course for more than an hour after the aircraft was dropped from the secondary radar. Subsequently, an even later investigation of satellite data indicated that the aircraft continued to fly at high speeds and at a high altitude for six hours after it disappeared from secondary radar. Ultimately it is believed to have crashed into the Indian Ocean [1].

The inability to locate the MH370 aircraft brings to light the challenge of finding a (reasonably sized) metallic airplane in the ocean. Sonar may sometimes be used when the target of interest is sufficiently noisy. Alternatively, over short ranges, magnetic anomaly detectors may be employed [2]. In general, electromagnetic detection is not used due to the high attenuation rate of electromagnetic waves in the conductive ocean. With an average electrical conductivity of ~3.3 S/m, the skin depth of the ocean is just 27 m at 100 Hz, and it is even shallower at higher frequencies. Note that the average depth of the ocean is ~3.5 km.

The possibility of conducting remote-sensing studies in the ocean using frequencies below 100 Hz in the ultra-low frequency (ULF: < 3 Hz) and extremely low frequency (ELF: 3 Hz – 3 kHz) range opens up new detection possibilities because of the increased skin depth. These frequencies have been previously considered (e.g. [3-9]). However, most of these studies focused on electromagnetic sources located on land or in the air region above the ocean [3-8]. One study investigated electromagnetic propagation between source and receiver antennas both located in seawater, however frequencies of 100 kHz and 14 MHz were used, which provided ranges of just 300 m [9].

In this Paper, the feasibility of using subsea cables as a source of ULF/ELF electromagnetic waves for remote-sensing of the oceans is considered for the first time. The motivation for using subsea cables is as follows: (1) they already exist in many locations around the world, and (2) they are electrically long, even at ULF/ELF, due to the shortening of electromagnetic wavelengths in the ocean.

With respect to (1), sub-sea cables are extensively utilized for international communication purposes, with over 400 cables in operation around the world that collectively span over 1.2 million km. Additionally, there are many older cables no longer in service but still located along the ocean floor. In most cases, the undersea cables are simply laid on the ocean floor. Closer to shore, cables may be buried under the seabed for protection.

Concerning (2) above, the electromagnetic

Submitted On: March 10, 2021
Accepted On: April 25, 2021
https://doi.org/10.47037/2020.ACES.J.360501

wavelength at a frequency of 10 Hz is shortened from ~30 Mm in the air to just 548 m in the ocean. At 0.1 Hz, the wavelength is shortened from ~3,000 Mm in the air to 5.48 km in the ocean. As a result, long undersea cables are expected to radiate much more efficiently at the bottom of the ocean compared to a comparable antenna located in the air or on land. For example, the Navy's ELF transmitter, having two 22.5-km long lines over land in Wisconsin and Michigan and having a third line over land in Michigan that was 50 km long, was known to have very poor radiation efficiency at 76 Hz until it was turned off in 2004 [10].

The goal of this paper is to computationally test the feasibility of using undersea cables as a source in a ULF/ELF remote-sensing system used to detect airplanes submerged in the ocean. Three-dimensional finite-difference time-domain (FDTD) [11, 12] models are used to model a realistic bathymetry, the cable source, the resulting ULF/ELF propagation, and the scattering caused by the object (airplane). First, the remote-sensing system is tested at multiple frequencies in the ULF/ELF band to determine an optimal operating frequency. Subsequently, the object is moved around in the vicinity of the cable to examine the total field perturbation caused by the object.

Section II describes the first FDTD model (Model #1) that is used to obtain the optimal operating frequency. Section III discusses the possibility of detecting the object and analyzes the results relative to the background noise level and measurement capabilities of present-day magnetometers. Section IV studies the effect of the ocean floor. Section V describes a second FDTD model (Model #2) that that is equivalent to Model #1 but extends over a larger area, is more computationally efficient, and includes a more realistic bathymetry. Section VI presents results from Model #2 with the aircraft located on the ocean floor at various distanced from the undersea cable, and then also results for the aircraft elevated above the ocean floor (representing it sinking). Section VII summarizes and concludes the Paper.

II. FDTD MODEL DESCRIPTION

The first FDTD model (called Model #1) is used to find the optimal operating frequency by comparing the propagation attenuation rate of the scattered fields from the object with the background noise level and magnetometer sensitivity level. Model #1 extends 5 km in the X-, Y-, and Z-directions and has a grid resolution of 15 m in each Cartesian direction. This grid resolution is sufficiently high to account for the wavelengths and skin depth of the modeled electromagnetic waves ranging from 0.1 to 100 Hz.

As shown on the left side of Fig. 1, the top half of the grid in the Z-direction consists of ocean water having a conductivity of $\sigma = 3.3$ S/m and a relative permittivity of $\varepsilon_r = 81$. The bottom half of the grid models the ground having a conductivity of $\sigma = 0.01$ S/m (a conductivity for ground under the ocean as obtained from [13]) and a relative permittivity of $\varepsilon_r = 15$. Thus, in Model #1, the ground is assumed to be flat. Both the ground and ocean are homogeneous in the XY plane.

We note that in cold, deep ocean water, the conductivity of the ocean is ~2.5 S/m, and that in warmer surface ocean water, the conductivity is ~6 S/m [14]. Since this work is focused on ULF propagation in colder, deeper ocean waters (but not the deepest parts of the ocean), we used a value of $\sigma = 3.3$ S/m. The impact of accounting for the varying ocean conductivity in an FDTD model that extends from more than 2 km below the surface of the ocean and up into the atmosphere is presented in Fig. 12 of [4]. As expected, higher ocean conductivity values increase the attenuation of the ULF waves.

The undersea cable source is assumed to have a sinusoidal current of frequency 0.1, 1, 10, or 100 Hz with an amplitude of $I = 10$ mA. The cable is modeled as an infinitely-long current density source immediately above the ground, as shown in Fig. 1. Specifically, the cable source is modeled along a string of electric field components oriented in the X-direction (E_x) and across the entire length of the grid. Periodic boundary conditions (PBC) are used on the -X and +X edges of the grid to make the cable infinitely long in the X-direction. This is implemented by copying the last layer of updated, tangential electric field values on the +X side of the grid to the first layer of stored (not updated) electric field values on the -X side of the grid:

$$E_t(1,:,:) = E_t(imax,:,:). \quad (1)$$

This is performed immediately after the $E_t(imax,:,:)$ components are updated. Also, the magnetic fields are copied in the reverse direction; the first layer of updated tangential magnetic fields on the -X side of the grid are copied to the +X side of the grid:

$$H_t(imax,:,:) = H_t(1,:,:). \quad (2)$$

This is performed immediately after the $H_t(1,:,:)$ components are updated.

When the object is added to the grid, however, the periodic boundaries in the X-direction cause the object to be modeled as a periodic array in the X-direction. Therefore, the FDTD grid is extended over a considerable distance in the X-direction (5 km) to allow sufficient attenuation of the electromagnetic scattering from the mirrored objects, so that they do not influence the calculation of the scattered fields from the primary object of interest.

The other edges of the grid in the Y- and Z-directions employ surface impedance boundary conditions (SIBC)

to save computational space for each material. The Beggs method is used to formulate the SIBC for the ocean ground and ocean water [15], where the tangential electric fields on the same side of the boundary as the FDTD grid are updated using:

$$\vec{E}_t(n\Delta t) = \eta_2\left[\hat{n} \times \overrightarrow{H_t}(n\Delta t)\right] - \sum_{i=1}^{L} A_i(n\Delta t), \quad (3)$$

where n is the time step number, Δt is the time step increment, η_2 is the impedance of the ocean/ground boundary, L denotes the number of first-order rational functions used in the approximation (a value of 6 was used),

$$A_i(n\Delta t) = p_{i1}\left[\hat{n} \times \overrightarrow{H_t}(n\Delta t)\right] + p_{i2}\left[\hat{n} \times \overrightarrow{H_t}((n-1)\Delta t)\right] + p_{i3}\, A_i((n-1)\Delta t), \quad (4)$$

and

$$p_{i1} = \eta_2 \frac{C_i}{\omega_i}\left[1 + (e^{-a\omega_i \Delta t} - 1)/(\Delta a \omega_i)\right], \quad (5)$$

$$p_{i2} = \eta_2 \frac{C_i}{\omega_i}\left[\frac{1}{(\Delta t a \omega_i)} - e^{-a\omega_i \Delta t}\left(1 + 1/(\Delta t a \omega_i)\right)\right], \quad (6)$$

$$p_{i3} = e^{-a\omega_i \Delta t}, \quad (7)$$

where $a = \sigma_2/\varepsilon_2$, and the six values used for C_i and ω_i are provided in Table 1 of Ref. [15]. Please see Ref. [15] for more details. Additional simulations not shown here demonstrate that extending the grid out further in the X-, Y-, and Z-directions does not alter the results for the primary object of interest.

The object has a conductivity of $\sigma = \mathbf{1} \times \mathbf{10^7}$ S/m (on the same order as many metals) and resides on many electric field components in the shape of a cylinder with a diameter of 60 m and a length of 60 m.

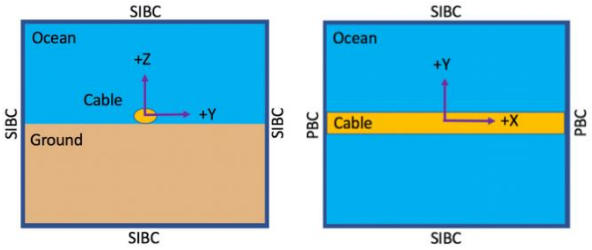

Fig. 1. Schematic diagram of Model #1 without the object. On the left is a view of the YZ-plane at the center of the FDTD grid in the X-direction. The diagram shows the ocean (blue), ground below the ocean (light brown), and the cable (yellow cylinder) located just above the ocean floor. PBCs are utilized on the X-direction edges of the grid, and SIBCs are used on the other four edges of the grid. On the right is a view of the XY-plane just above the ground and through the center of the cable.

III. DETECTABILITY AND FREQUENCY STUDY

A. Scattering calculation

To determine the optimal operating frequency for the remote-sensing system, the scattering from the object is first obtained for different cable source frequencies. Model #1 is run with no object. Then it is re-run with the object located horizontally away from the cable source at a distance of 2 km (on the ground). Several possible operating frequencies are tested to compare the scattering attenuation rates away from the object. Specifically, 0.1, 1, 10, and 100 Hz are tested. For each frequency, the simulation is run for a different number of time steps to ensure that steady-state conditions are reached all the way out to the edges of the grid. For example, the 100 Hz source is run for 25 wavelengths compared to just half of a wavelength for the 0.1 Hz source.

The scattering from the object is obtained by comparing the results from the simulation having the objects vs. the simulation without the object. Specifically, the total magnetic density field perturbation, ΔB, at any position of interest (X, Y, Z) is obtained from (8) by calculating the difference between the total magnetic flux density from the simulation having the object (B^{Obj}) vs. the simulation without the object ($B^{\text{No O}}$):

$$\Delta B(X,Y,Z) = B^{\text{Obj}}(X,Y,Z) - B^{\text{No Obj}}(X,Y,Z), \quad (8)$$

where

$$B^{\text{Obj}}(X,Y,Z) = \sqrt{\begin{aligned}&\left(B_X^{\text{Obj}}(X,Y,Z)\right)^2 \\ &+\left(B_Y^{\text{Obj}}(X,Y,Z)\right)^2 \\ &+\left(B_Z^{\text{Obj}}(X,Y,Z)\right)^2,\end{aligned}} \quad (9)$$

and

$$B^{\text{No Obj}}(X,Y,Z) = \sqrt{\begin{aligned}&\left(B_X^{\text{No O}}(X,Y,Z)\right)^2 \\ &+\left(B_Y^{\text{No O}}(X,Y,Z)\right)^2 \\ &+\left(B_Z^{\text{No O}}(X,Y,Z)\right)^2.\end{aligned}} \quad (10)$$

All of the ΔB results are plotted on a log base 10 scale according to:

$$\Delta B_{\log}(X,Y,Z) = \log_{10}(|\Delta B(X,Y,Z)|). \quad (11)$$

B. Background Noise Level (BNL) and Detection Limit (DL)

To investigate the feasibility of using the remote-sensing system in a real-world scenario, the field perturbations caused by the object are compared to the background noise level (BNL) to see how far away an object may be detected at each frequency. Figure 2 displays the magnetic background noise level over a wide range of frequencies in the air region of the Earth-ionosphere waveguide [16]. Figure 2 shows measured data along with a fitted curve.

According to Snell's Law, any electromagnetic wave propagating in the air region will propagate nearly perfectly downward in the ocean after crossing the air-ocean interface. Thus, the background noise level at

depth in the ocean may be obtained by taking the BNL in the air and attenuating it according to plane wave theory with depth in the ocean. Table 1 provides the BNL for the magnetic flux density in the air region and then also the corresponding attenuated magnetic flux density at a depth of 3 km below the ocean surface (roughly the average depth of the ocean). The scaling law equation from [16] (see the caption for Fig. 2) provides the BNL in the air assuming the receiver bandwidth is equal to the center frequency of the source.

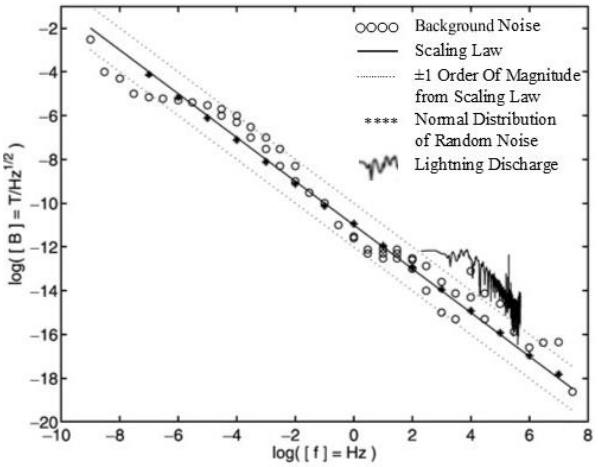

Fig. 2. The measured magnetic field spectrum of the background noise from ~10-9 Hz to ~107 Hz (circles) which can be approximated by the scaling law (solid line) B = B0(f0/f) where B0 ≈ 10−11 T/Hz1/2, f0 = 1 Hz is a scaling constant, and f is the frequency of the magnetic field. The measured magnetic field exhibits deviations from the scaling law by ∼±1 order of magnitude across the entire frequency range (dotted lines). The scaling law is simulated in the frequency range from 10−7 Hz to 107 Hz with a persistent normal distributed random noise process (stars) and exhibits an excellent agreement with the scaling law. The noisy solid line is measured data from a lightning discharge. (Courtesy of Ref. [16]).

Table 1: Background noise levels at different frequencies

Frequency	BNL in the Air Region	BNL at 3 km Depth in the Ocean
0.1 Hz	0.316 nT	0.0117 nT
1.0 Hz	1.00e-2 nT	2.04e-7 nT
2.0 Hz	3.55e-3 nT	8.01e-10 nT
10.0 Hz	3.16e-4 nT	3.28e-19 nT
100.0 Hz	1.00e-5 nT	5.07e-53 nT

To investigate the feasibility of using the remote-sensing system in a real-world scenario, the field perturbations caused by the object are compared to the sensitivity of a sensor that may be used. For this study, a superconducting quantum interference device (SQUID) magnetometer is considered for detecting the perturbation. SQUID sensors are based on superconducting loops containing alternating current Josephson junctions. The SQUID is inductively coupled to a resonant tank circuit, and the effective inductance of the tank circuit changes depending on the external magnetic field, thus changing the resonant frequency of the tank circuit. SQUIDS have been used in oil exploration, mapping tectonic faults, biomedical imaging, and in military applications [18]. SQUIDs are known to have a detection limit (DL) on the order of $fT/\sqrt{Hz}$ [17]. In Table 2 is listed the range of source frequencies and the associated DL for a SQUID magnetometer.

Table 2: Detection limit for SQUID magnetometers at different frequencies

Frequency	Detection Limit (DL)
0.1 Hz	3.1e-6 nT
1.0 Hz	1.0e-6 nT
10.0 Hz	3.1e-7 nT
100.0 Hz	1.0e-7 nT

C. Results

The BNL and DL values are now compared with the FDTD-calculated perturbations caused by the object. In Fig. 3, the scattering from the object at each source frequency is plotted in the Y-direction along a line through the center of the object (at X = 0, Z = 0). The object is placed at Y = 2 km away from the cable on the ground (at X = 0, Z = 0). The cable source is assumed to carry 10 mA. At each frequency, a horizontal line indicates the larger of the two values obtained from Table 1 (BNL) or Table 2 (DL) are plotted (so, the BN level is indicated for 0.1 Hz, and the DL level is indicated for 1, 10, and 100 Hz). For the object to be detectable, the scattered total magnetic density caused by the object must be above the corresponding horizontal line.

Examining the results in Fig. 3, at 1, 10, and 100 Hz the scattering from the object is detectable above the BNL and DL at distances away from the object. However, the scatterings at 100 Hz are only detectable within a few hundred meters of the object, and the scatterings at 10 Hz are detectable at distances of < 1 km. Thus, ~1 Hz is determined to be an optimal frequency for detecting a 60-m diameter and 60-m long object on the ocean floor.

Considering the values in Tables 1 and 2 and the results in Fig. 3, the detectability of the object may be improved if: (1) the cable source can carry more than 10 mA; or (2) more sensitive magnetometers may be employed.

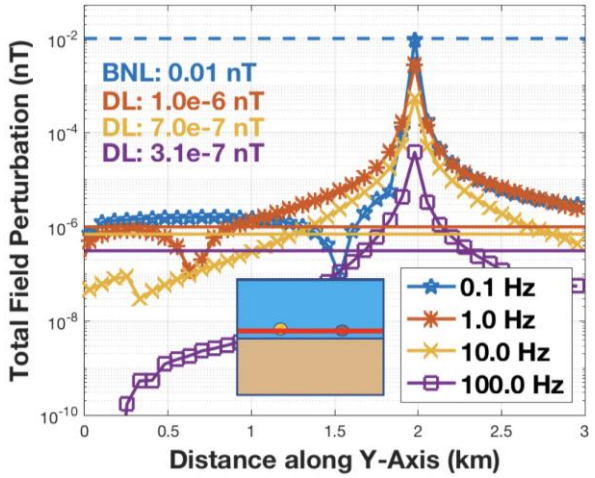

Fig. 3. Scattered total magnetic flux density from the object located at Y = 2 km and at the different source frequencies. Also included is a horizontal line indicating the larger of the two values obtained from Tables 1 and 2 at each frequency: the background noise level (BNL, shown as a dashed horizontal line) at a depth of 3 km in the ocean or the detection limit (DL, shown as a solid horizontal line) of a SQUID magnetometer.

IV. OCEAN FLOOR

Before different positions of the object are considered, Model #1 is used to study the effect of the ocean floor on the detectability of the object. The ocean floor is expected to play a role in the electromagnetic propagation from the cable source and the scattering from the object, since both the cable and object of interest are located directly on the ocean floor.

For this study, the same Model #1 is rerun at 1 Hz as for the results in Fig. 3, except that the ground is removed and it is replaced with ocean (it is an all-ocean model). Figure 4 superimposes the difference in the total magnetic flux densities at 1 Hz from Fig. 3 (with ground) with the corresponding results obtained from the two all ocean simulations (run with and without the object). As shown in Fig. 4, the ground plays a huge role in the total scattered magnetic flux densities when the source and scattering object are on the ground.

V. MODEL #2

A lower-resolution model (Model #2) is now used to perform simulations at the optimal frequency of 1 Hz. Model #2 is the same as Model #1 except for three changes:

(1) The grid resolution is 60 m in each Cartesian direction rather than 15 m. This 60-m resolution is still sufficient to capture the size of the object, the 1.7 km electromagnetic wavelength, and the 275 m skin depth at 1 Hz in the ocean, but it relaxes the computational requirements.

(2) Model #2 covers a larger spatial region, namely 7.4, 10.8, and 9.0 km in the X-, Y-, and Z-directions, respectively. This allows the object to be placed at further distances from the cable.

(3) The object size remains the same, but only one electric component (E_x) is used to model the object at the lower grid resolution.

Models #1 and #2 have been shown to provide identical results for the 1 Hz result shown in Fig. 3 (not shown here).

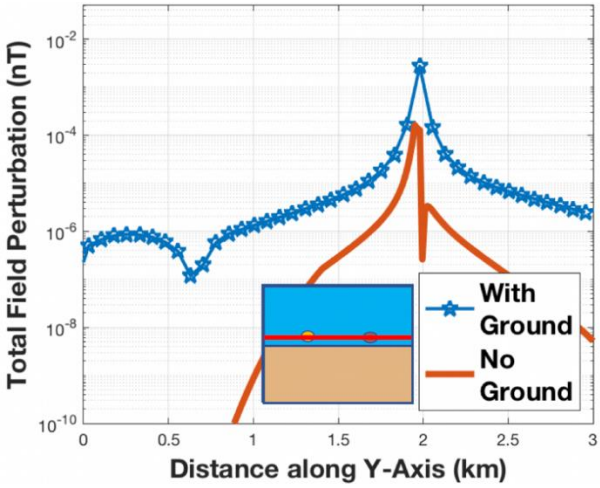

Fig. 4. Scattered total magnetic flux density from the object located at Y = 2 km and at 1 Hz for Model #2 (including the ground as in Fig. 3) and then for the case wherein the ground is replaced with ocean (an all-ocean model). The ground causes a significant amount of reflection allow more scattering from the object.

VI. SCATTERING

Model #2 is now used to obtain scatterings from the object located at different positions relative to the cable source. A realistic bathymetry is added for the ocean floor. Figure 5 displays the 2D and 1D plots of the bathymetry added to Model #2. The bathymetry data is a survey off the eastern coast of the U.S. The data is directly from the NOAA National Centers for Environmental Informational website (U.S. Coastal Relief Model Vol. 21). To obtain the perturbation from the scattering object, two sets of simulations are run as in Section III: the model is run with the object and then without the object. Equations (8) and (11) are used to

[1] https://www.ngdc.noaa.gov/mgg/coastal/grddas02/html/gna37075.htm

calculate the perturbation as the object is placed at various locations in the model.

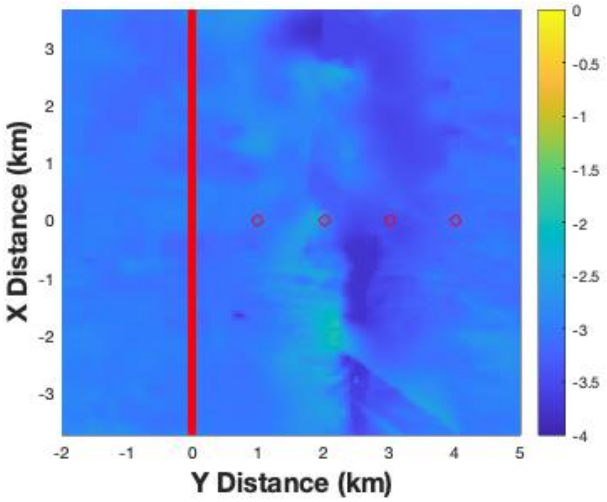

(a)

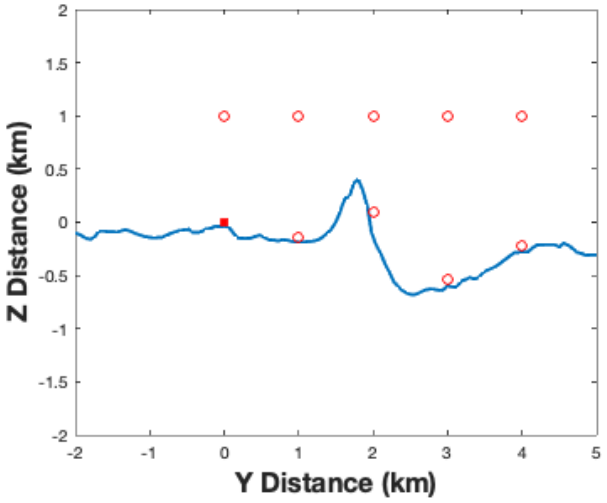

(b)

Fig. 5. (a) 2D top view of the bathymetry used in Model #2. The color scale refers to the elevation depth from the ocean surface. The red line represents where the cable source is located. The red circles illustrated where the scattering object is located for each simulation. (b) Is a 1D plot extending through the cable and scattering object locations of (a) in order to show in more detail the variance of the ocean floor.

Figure 6 illustrates the steady-state magnetic flux density values at 1 Hz (maximum magnetic flux densities achieved over all time steps at each grid cell). As expected, the 1 Hz wave attenuates faster in the ocean ($Z \geq 0$ km) than in the ground ($Z < 0$ km) due to the higher conductivity of the ocean. Also seen in Fig. 6 is that the much lower attenuation rate in the hill to the right of the cable makes up for the relatively high reflection coefficient between the ocean/ground and ground/ ocean interfaces. Also, there is diffraction around the hill. This means that there are higher amplitudes observed in the ocean on the far side of the hill relative to when there is a flatter ground (as on the left side of the cable).

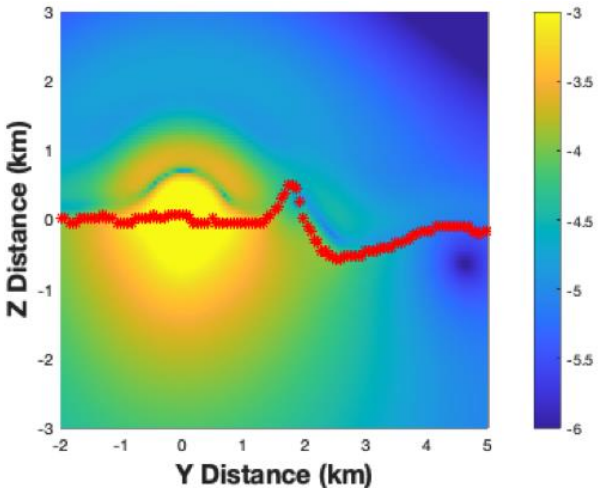

Fig. 6. A YZ-plane of the grid at X = 0 of the steady-state total magnetic flux density amplitudes with no object present plotted on a log base 10 scale. The cable source is located at (Y=0, Z=0). The units are in nanoTelsa. The red markers indicate the ocean floor.

A. Object on the ground

For the first simulation, the object is placed on the ocean floor at a distance of 1 km from the cable source. The simulation with the object is rerun three more times, with the object moved each time in 1 km increments away from the source until it reached 4 km (when the object is at Y = 2, the simulation scenario matches that of Fig. 3). Figure 7 shows the placement of the object for each of these four simulations.

Figure 8 shows a YZ-plane of total magnetic density field perturbation values at X = 0 on a log scale as calculated from (11) with the cable source at (Y=0, Z=0) km and the object at (X=0, Y=1, Z=0) km. The presence of the object is clearly visible, as well as the interaction of the scattering caused by the object with the ground and cable.

Figures 9 – 11 plot the total magnetic density field perturbation on a log scale as calculated by (11) for all four positions of the object along the ground. Figure 9 plots the perturbation along the Y-direction at X = 0 and Z = 0. As expected, the peak amplitude of $\Delta B_{\log}$ decreases as the object is moved further from the cable source. Comparing the magnitudes of the four peaks in Fig. 9, as well as additional simulations for a flat ground, the presence of the hill does not diminish the detectability of the object (at 1 km vs. further distances). Also, note that the electromagnetic wavelength in the

ocean water at 1 Hz is just 1.7 km, so when the object is at a distance of 1 km, it is in the near field of the cable.

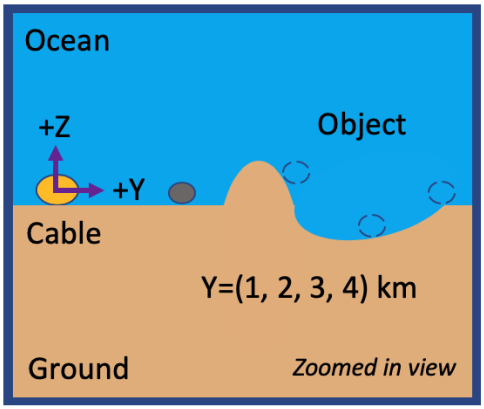

Fig. 7. Zoomed-in diagram illustrating where the object (gray and dashed circles) is placed in each simulation. In four separate simulations, the object is placed on the ocean floor starting 1 km away from the cable and then it is moved further away in increments of 1 km. The object is represented by grey and dashed circles to indicate that only a single object is included in each simulation.

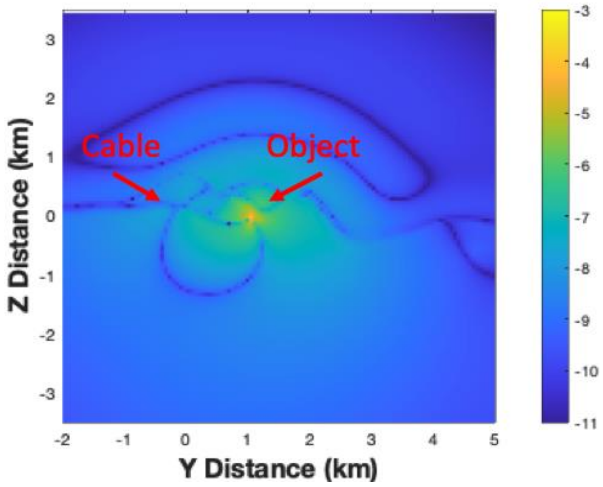

Fig. 8. A YZ-plane at X = 0 of $\Delta B_{\log}$ as calculated by Eq. 2. The object is placed at (X=0, Y=1, Z=0) km, and the cable is at (Y=0, Z=0) km in the image. The units are in nanoTesla. Note that the color scale is the same as in Fig. 6.

Figure 10 plots the perturbation along the X-direction at Z = 0 and through the center of the object. The background noise level (BNL) and magnetometer sensitivity limit (SL) from Tables 1 and 2 are plotted for comparison. Finally, Fig. 11 plots $\Delta B_{\log}$ along the Z-direction at X = 0 and through the center of each object. Negative Z positions correspond to positions in the ground.

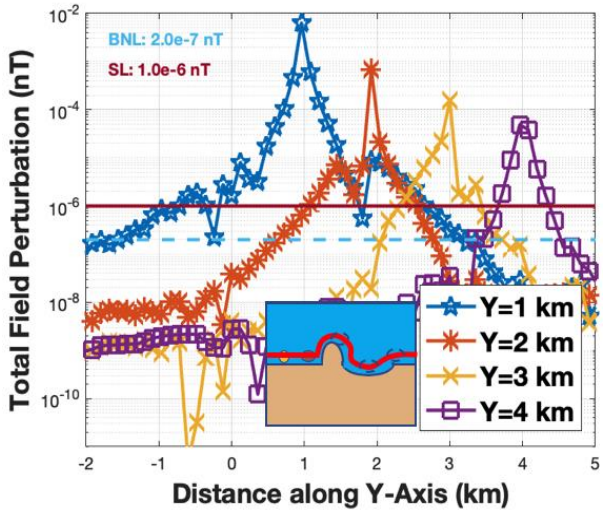

Fig. 9. Zoomed-in 1-D plots of $\Delta B_{\log}$ from four separate FDTD simulations with the object at distances of 1, 2, 3, and 4 km away from the cable source in the Y-direction and immediately above the ground. The values are plotted along the Y-direction along the red line shown in the diagram inset. The legend Y values correspond to the location of the object. The dash (BNL) and solid (SL) lines are the background noise level and sensor limits.

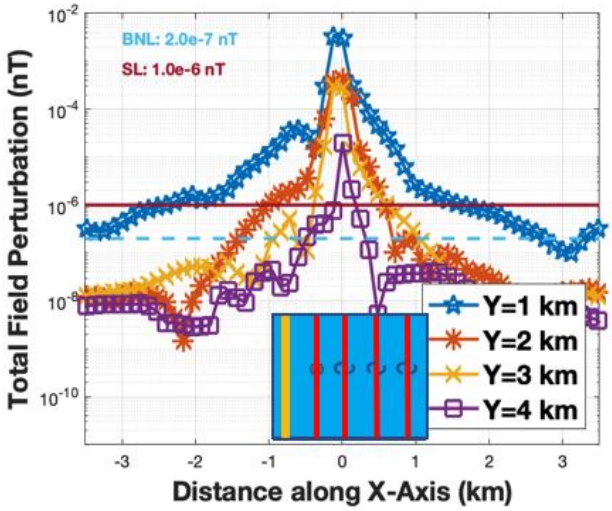

Fig 10. Same as Fig. 9, but now plotted along the X-direction at Y = 1, 2, 3, and 4 km and Z = 0 km. The legend Y values correspond to the location of the object.

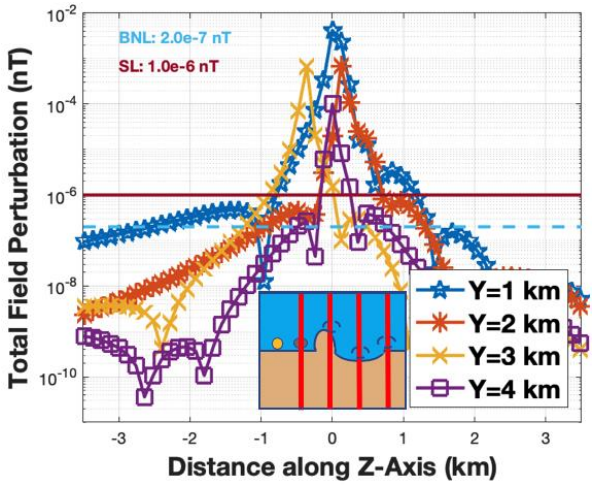

Fig. 11. Same as Fig. 9, but now plotted along the Z-direction at Y = 1, 2, 3, and 4 km and at X = 0 km. The legend Y values correspond to the location of the object.

B. Object 1 km above the ground

Following the same procedure as in Section A, Model #2 is now rerun with the object elevated 1 km above the ocean floor. First, the object is placed immediately above the cable source. The simulation with the object is then rerun four more times, with the object moved in 1 km increments horizontally away along the Y-direction. Figure 12 shows the placement of the object for each of these five simulations.

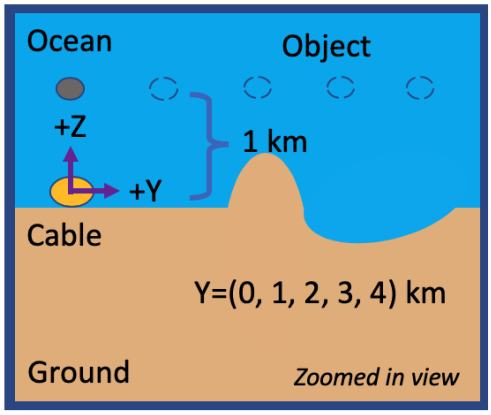

Fig. 12. Zoomed-in diagrams illustrating where the object (gray and dashed circles) is placed in each simulation. On the right side, in five separate simulations, the object is placed 1 km above the ocean floor. The object is initially positioned directly above the source and then it is moved horizontally away in the Y-direction in increments of 1 km. The object is represented by grey and dashed circles to indicate that only a single object is included in each simulation.

Figures 13 and 14 plot the total magnetic density field perturbation on a log scale as calculated by (11) for all five positions of the object. Figure 13 plots $\Delta B_{\log}$ along the Z-direction at X = 0 and through the center of each object. Figure 14 plots the perturbation along the Y-direction at X = 0 and Z = 1 km. Again, as expected, the peak amplitude of $\Delta B_{\log}$ decreases as the object is moved farther from the cable source.

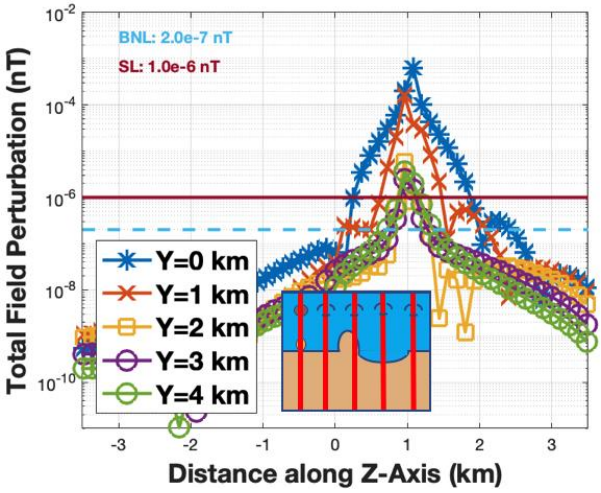

Fig. 13. Zoomed-in view of $\Delta B_{\log}$ from five separate FDTD simulations with the object 1 km above the ground and 0, 1, 2, 3, and 4 km away from the source in the Y direction. The values are recorded in the Z-direction along the red lines of the diagram inset. The legend Y values correspond to the location of the object and Y-position of the recorded data. The dash (BNL) and solid (SL) lines are the background noise level and sensor limits.

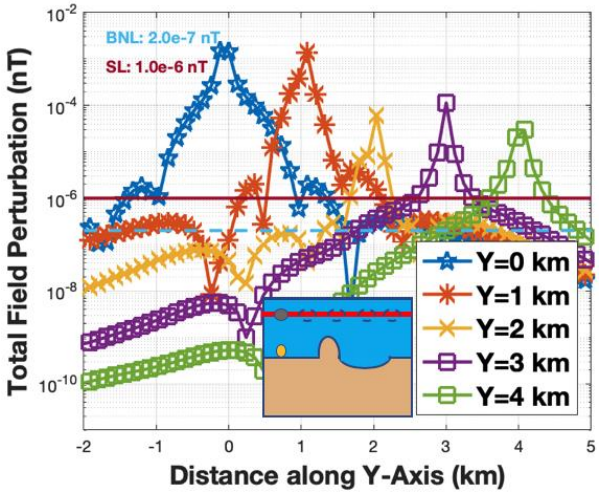

Fig. 14. Same as Fig. 13, but now along the Y-direction at X = 0 and Z = 1 km. The legend Y values correspond to the location of the object. The dash (BNL) and solid (SL) lines are the background noise level and sensor limits.

C. Discussion

The results in Sections A and B are now used to design a possible detection system. Using an undersea cable operating with 10 mA and at a frequency of 1 Hz, the object on the ground is observed to be detectable at distances of at least 4 km from the cable source. From Fig. 9, sensors would need to be placed at 1 km increments on the ground away from the cable in the Y-direction in order to detect the scatterings from the object above the BNL and the DL of the sensor. From Fig. 10, the sensors would also need to be in 1 km increments in the X-direction at Y distances up to 2 km, but then every ~500 meters between 2 and 4 km. The possible sensor array that accounts for the results from both Figs. 9 and 10 is shown in Fig. 15. Each sensor location would have one 3-axis SQUID magnetometer.

The above analysis assumes the object is parallel to the cable. The spacing of the sensor array may need to be closer to 500 meters at all distances from the cable and in both the X- and Y-directions if the object is always oriented perpendicularly to the cable.

From Fig. 13, none of the (sinking) objects 1 km above the ground are detectable on the ground, however, it would be possible to detect the sinking objects 1 km above the ground using sensors floating 1 km above the ocean floor. Therefore, this detection system is ideal for sunken airplanes and ships that lay on the ocean floor.

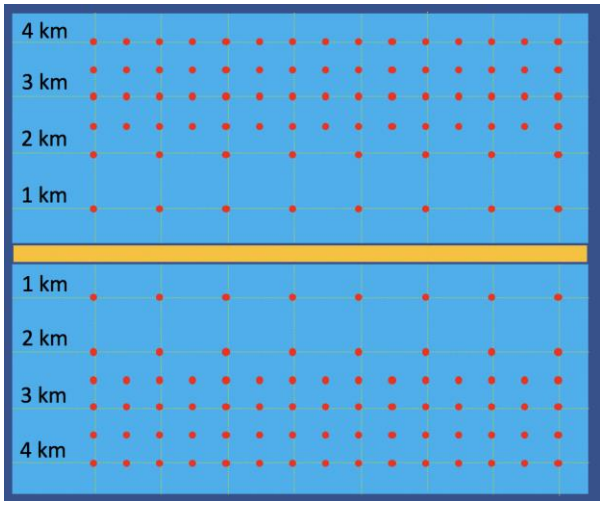

Fig. 15. Proposed sensor array for sensors (red circles) located on the ground and used to detect objects on the ground or located a relatively short distance above the ground.

IV. CONCLUSION

Remote sensing of airplanes that have crashed into the ocean is challenging due to the short skin depth of the electromagnetic fields, especially at frequencies above 100 Hz. In this Paper, a remote-sensing system is proposed that would involve three steps: (1) a subsea cable would be used to generate electromagnetic waves at 1 Hz; (2) the electromagnetic waves from the source would propagate in the ocean water and scatter off of objects (submerged airplanes modeled as being 60 m long and having a diameter of 60 m), thereby perturbing the background magnetic fields; and (3) the scatterings off of the objects would be detected by an array of sensors (spaced 1km apart closer to the cable and 500 further away from the cable) on the ocean floor. This proposed remote-sensing system would detect any of the sunken metallic objects within at least 4 km horizontally away from the cable. Note, however, that the spacing of the sensors may need to be slightly adjusted when the ocean conductivity in the vicinity of the sensors is different than the assumed 3.3 S/m used in this Paper (i.e., the sensors may be spaced farther apart when the ocean conductivity is lower than 3.3 S/m).

3-D FDTD models were used to design this remote-sensing system. Specifically, they were used to obtain the total magnetic flux density field perturbation from the object located at various distances and positions from the cable. The total field perturbation was extracted by running the model first without and then with the object. The FDTD models were also used to determine the optimal operation frequency for the remote-sensing system (1 Hz), which provides detection capabilities over the largest distances from the source and also permits the sensors to be located as far apart as possible. A separate simulation showed that for objects located on the ground, the presence of the ground improves the detectability of the object.

The FDTD-calculated scatterings caused by the object were compared with the expected background noise level of the magnetic flux density in the ocean. They were also compared with the sensitivity of a SQUID magnetometer. For the object to be detectable, the magnitude of the scatterings would need to be above the BNL and DL of the sensor. Detectability could possibly be improved by separately analyzing the magnitude of each Cartesian component of the magnetic flux density with the expected background noise level. Detectability could also be improved by increasing the current carried by the cable, and by using more sensitive sensors.

It is expected that the scatterings from an object would be dependent on its size. For this study, the object that was modeled is 60 meters in diameter and in length. Larger objects should generate larger scatterings and should be detectable at farther distances from the cable and with sensors spaced farther apart. Smaller objects would be expected to generate smaller scatterings. Future work could investigate the effect of having different sized objects.

ACKNOWLEDGMENT

The authors gratefully acknowledge the Center for

High Performance Computing (CHPC) at the University of Utah for providing supercomputing resources.

REFERENCES

[1] K. S. Yee, "Numerical solution of initial boundary value problems involving Maxwell's equations in isotropic media," *IEEE Trans. Antennas Propagat.*, vol. AP-14, pp. 302-307, 1966.

[2] W. Langewiesche, "What really happened to Malaysia's missing airplane," *The Atlantic*, July 2019.

[3] T. R. Clem, "Superconducting magnetic gradiometers for underwater target detection," *Nav. Eng. J.*, vol. 110, no. 1, pp. 139-149, Jan. 1998.

[4] R. W. P. King, "Lateral electromagnetic waves from a horizontal antenna for remote sensing in the ocean," *IEEE Trans. Antennas Propagat.*, vol. 37, pp. 1250-1255, Oct. 1989.

[5] D. R. Smith, S. Burns, J. J. Simpson, and S. M. Ferone, "FDTD modeling of scattered ultra-low frequency electromagnetic waves from objects submerged in the ocean," *IEEE Trans. Antennas Propagat.*, vol. 64, pp. 2534-2541, 2019.

[6] R. W. P. King, "Propagation of a low-frequency rectangular pulse in seawater," *Radio Science*, vol. 28, pp. 299-307, June 1993.

[7] R. W. P. King and S. S. Sandler, "The detection of dielectric spheres submerged in water," *IEEE Trans. Geosci. Remote Sens.*, vol. 30, pp. 892-896, Sept. 1992.

[8] R. W. P. King, "The propagation of a Gaussian pulse in seawater and its application to remote sensing," *IEEE Trans. Geosci. Remote Sens.*, vol. 31, no. 3, pp. 595-605, May 1993.

[9] M. Birsan, "Remote Sensing of 3-D conducting objects in a layered medium using electromagnetic surface waves," *IEEE Geosci. and Remote Sens. Let.*, Papers 4(4), pp. 561-565, 2007.

[10] M. Siegel and R. W. P. King, "Electromagnetic propagation between antennas submerged in the ocean," *IEEE Trans. Antennas Propagat.*, vol. 4, pp. 507-513, 1973.

[11] "Extremely Low Frequency Transmitter Site, Clam Lake, Wisconsin," (PDF). *Navy Fact File. United States Navy. 28 June 2001. Retrieved 17 February 2012 – via Federation of American Scientists.*

[12] S. Yee, "Numerical solution of initial value problems involving Maxwell's equations in isotropic media," *IEEE Trans. Antenna Propag.*, vol. 17, pp. 585-589, 1966.

[13] A. Taflove and S. Hagness, "Electrodynamics Entering the 21st Century" in C*omputational Electrodynamics: The Finite Difference Time-Domain Method*, 3rd ed., Norwood, MA, USA: Artech House, 2005.

[14] P. Bannister, "ELF propagation update," *IEEE J. Oceanic Eng.*, vol. OE-9, no. 3, pp. 179-188, 1984.

[15] S. Maus, "Electromagnetic ocean effects," in *Encyclopedia of Geomagnetism and Paleo-magnetism*, New York, NY, USA: Springer, 2007, pp. 740-742.

[16] J. Beggs, "Finite-difference time-domain implementation of surface impedance boundary condition," *IEEE Trans. Antenna Propag.*, vol. 40, no. 1, Jan. 1992.

[17] M. Füllekrug and A. C. Fraser-Smith, "The earth's electromagnetic environment," *Geophys. Res. Letts.*, 38, L21807, 2011. Doi: 10.1029/2011GL049572, 2011.

[18] M. Buchner, K. Hofler, B. Henne, V. Ney, and A. Ney, "Tutorital: Basic principles, limits of detection and pitfalls of highly sensitive SQUID magnetometry for nanomagnetism and spintronics," *J. Appl. Phys.*, 124, 161101, 2018.

[19] E. Mendenhall, "Shifting grounds: Scientific and technological change and international regimes for the ocean and outer space," *Ph.D. Dissertation*, Submitted to Johns Hopkins University, June 2017.

Dallin R. Smith received the B.S. in Physics from Brigham Young University, Provo, UT, USA, in 2016, and the M.S. and Ph.D. degrees in Electrical Engineering from the University of Utah, Salt Lake City, UT, USA, in 2019 and 2020, respectively. He is a Research Engineer in the Geospace Environment Impacts and Application Branch with the Space Vehicles Directorate, Air Force Research Laboratory, Albuquerque, NM, USA.

Jamesina J. Simpson received the B.S. and Ph.D. degrees in Electrical Engineering from Northwestern University, Evanston, IL, USA, in 2003 and 2007, respectively. She is an Associate Professor in the Electrical and Computer Engineering Department, University of Utah, Salt Lake City, UT, USA. Her research lab encompasses the application of the full-vector Maxwell's equations finite-difference time-domain (FDTD) method to electromagnetic wave propagation spanning 15 orders of magnitude across the electromagnetic spectrum. In particular, her group specializes in electromagnetic wave propagation within the global Earth-ionosphere waveguide. She received a 2010 National Science Foundation CAREER award, the 2012 IEEE AP-S Donald G. Dudley, Jr. Undergraduate Teaching Award, the 2017 URSI Santimay Basu Medal, and the 2020 IEEE AP-S Lot Shafai Mid-Career Distinguished Achievement Award.